Validation of ECMWF water vapor analyses by airborne DIAL measurements in tropical regions

H. Flentje, A. Dörnbrack, G. Ehret, and A. Fix

DLR Oberpfaffenhofen, Institut für Physik der Atmosphäre

D-82230 Weßling, Germany

April, 2005

Short title: VALIDATION OF ECMWF WATER VAPOR BY DIAL

Abstract

Airborne Differential Absorption Lidar (DIAL) measurements of tropospheric water vapor and aerosol from Brazil to south Europe in mid-March 2004 are presented and compared to operational analyses of the European Center for Medium Range Weather Forecast (ECMWF). The two 2-D sections across the tropical and sub-tropical Atlantic (5°S–37°N) reveal two different meteorological regimes. South of 20°N the Hadley circulation is evident as a humid fountain near the equator with synoptic scale inflow below 4 km (16°N) to 8 km (0°N), upper tropospheric (UT) outflow till 15°N and a dry sub-tropical subsidence layer in between. The 2nd section along the north-west African coast is controlled by mid-latitude dynamics. A deep stratospheric intrusion is associated with the cyclonic shear along a trough from the Canary Islands towards Gibraltar. In the sub-tropical layer and the intrusion, H_2O mixing ratios $q \approx 0.01\text{-}0.1$ g/kg are measured while $q > 0.5$ g/kg is found in the lower tropospheric air having been lifted to UT levels. While at mid-latitudes very low q is associated with thin particle filaments, the tropical free troposphere is nearly particle free.

On large scales the dynamical features and the water vapor mixing ratios are properly analyzed by the ECMWF at T511/L60 operational resolution. Local deviations arise from displacements of individual features, interpolation uncertainties, and small scale structures not resolved. The averaged q-difference in the lower and middle troposphere is below 10%. In the upper troposphere ECMWF values tend to be too high.

1. Introduction

Stratospheric water vapor alters the radiation balance (Forster and Shine, 1999), controls the formation of particles, particularly in the lowermost and the polar stratosphere thus affecting ozone depletion (Kirk-Davidoff et al., 1999). It seems to have an increasing trend (Oltmans et al., 2000), but the relevant source and loss mechanisms are yet not well understood. Transport across the tropical tropopause layer (TTL), commonly defined as the layer extending vertically from the level of main convective outflow at 10–14 km to the cold point tropopause, is regarded as the primary source of tropospheric constituents in the stratosphere. The amount of water vapor entering the stratosphere is limited by freeze drying of the ascending air within the coldest layer of the TTL (Sherwood and Dessler, 2000; Jensen and Pfister; 2004; Gettelman et al., 2004), but details of this dehydration mechanism are still subject of debate. In the stratosphere, the global-scale meridional redistribution of water vapor is largely maintained by two co-acting circulations, the thermally driven Hadley cell in the tropical troposphere and the planetary wave drag driven Brewer-Dobson residual stratospheric circulation which extends over the entire hemispheres (Brewer, 1949).

In the troposphere, water vapor is the most important greenhouse gas (Möller, 1963; Manabe and Weatherald, 1967; Shine and Sinha, 1991), the latent heat exchange involved in its phase changes affects the vertical stability, controls cloud formation (e.g. Kiehl and Trenberth, 1997; Koop et al., 2004; Kärcher, 2004) and the evolution of weather systems, making H_2O crucial for the energy balance of the global climate system (e.g. Chahine, 1992). Relative humidity controls radiative and chemical properties of aerosols and as the prime source of atmospheric hydroxyl radicals,

water vapor plays a key role in removing both, particles and trace gases from the atmosphere. In spite of the fundamental role of moist processes in the atmosphere H_2O constitutes only 2% of the atmosphere's mass. As its mixing ratio at a given location may rapidly vary over three orders of magnitude, accurate monitoring of water vapor, especially in the upper troposphere and lower stratosphere (UTLS) and in remote areas remains an important issue. Sensitive regions (e.g. at the westerly Atlantic or Pacific storm tracks) to which short-term forecast errors are most responsive and non-populated areas are only covered by a few radiosonde stations (Marseille and Bouttier, 2001). Moreover, radiosonde data do mostly not provide reliable water vapor at pressures p>300 hPa or in dry regions < 0.0622 g/kg[1] (100 ppmv). Therefore, satellite water vapor data (Moreau et al., 2003), typically from upper-air between 200 and 500 hPa but at relatively low spatial resolution and with considerable uncertainty, is being exploited at ECMWF for its potential to constrain the model humidity fields in these regions (Hólm et al, 2002).

Owing to its importance, accurate water vapor fields are essential for global climate studies. Frequently, reanalysis data (e.g. ERA 40) or operational meteorological analyses of the European Centre for Medium Range Weather Forecast (ECMWF) are used for atmospheric process studies or as input for chemical transport- and global chemistry-climate models. Several improvements to the ECMWF model system during the recent years allow present operational analyses to benefit significantly from humidity data also assimilated from microwave or infrared satellite borne sounders. Each different type of water vapor data improves the forecast on its own, not only in precipitation and water vapor but also in other prognostic variables

[1] Conversion of water vapor mixing ratio: $w_{H2O\ [g/kg]} = \varepsilon \times 10^{-3} \times w_{H2O\ [ppmv]}$, w_{H2O} being the mixing ratio in g/kg or

like geopotential and wind (Andersson et al., 2004). This points up the rapid progress compared to earlier model versions at ECMWF where assimilation of water vapor data seemed to have only negligible impact on the accuracy of water vapor fields (Bengtsson et al., 2004). Therefore, present efforts aim to include additional humidity data sources in assimilation schemes of numerical weather prediction (NWP) models which currently only use lower and middle tropospheric humidity from regular radiosonde soundings at pressures p>300 hPa (Elliott and Gaffen, 1991; Leiterer, 1997). An important issue with upcoming humidity data are biases since the analysis mostly only adds a few percent to the background fields of the assimilation scheme (increments are < 5% of the fields in general, larger somewhere). To define precise absolute background fields, standards for humidity observations are required. To this end, Differential Absorption Lidar (DIAL) observations can contribute, as their bias mainly depends on the accuracy of the H_2O spectral absorption cross sections and are little sensitive to atmospheric pressure and temperature. Regarding the importance of ECMWF water vapor fields, which closely interact with dynamics and precipitation, their validation by unbiased experimental data is highly desirable.

In a previous paper, we analyzed long-range flights along the northern Atlantic storm track in May/June 2002 and compared them to operational analyses of the ECMWF and to mesoscale simulations with the MM5 model (Flentje et al., 2005). During these flights relatively small scales and large water vapor gradients associated with deep stratospheric intrusions dominated. Considerable deviations were found. Here,

---

ppmv, respectively and ε=0.622 the ratio of molecular mass of water vapor to *dry* air. (1 g/kg ≡ 1608 ppmv)

we investigate H_2O and aerosol distributions across the (sub-)tropical Atlantic between Brazil and Europe (5°S to 37°N), measured in mid March 2004. The scales in sub-tropical and tropical regions are significantly larger. Measured and analyzed 2-D water vapor distributions along the DIAL flight track are compared with respect to scales, stationarity, origin and geographical location of observed structures. To this end, 6-hourly ECMWF operational analysis at T511 spectral resolution on 60 vertical levels and ECMWF-based backward trajectories are used.

Section 2 of this paper briefly describes the experimental procedure, the DIAL and the data evaluation, Section 3 shows the DIAL measurements in the context of ECMWF analyses and trajectories. In Section 4, the 2-D water vapor sections over the tropical and sub-tropical Atlantic are compared to the corresponding ECMWF analyses. Section 5 summarizes and concludes the paper.

2. Experimental setup and Diagnostic Tools

2.1. Transfer Flights

Long-range airborne Differential Absorption Lidar (DIAL) measurements of water vapor and particle backscatter ratio have been performed across the sub-tropical and tropical Atlantic from Fernando de Naronha, Brazil (5°S, 36°W) to South Spain (37.2°N, 6°W) on 14 and 15 March 2004, as outlined in Figure 1. The nadir looking lidar profiled the troposphere from ~10 km to the ground, covering northern hemisphere (NH) middle-, sub-tropical-, and tropical latitudes till about 5°S, roughly 8000 km one way with an intermediate stop in Sal (Cape Verde Islands).

2.2. Water Vapor DIAL

For the trans-Atlantic flights the DLR water vapor DIAL (Ehret et al., 1999; Poberaj et al., 2002) has been installed onboard the DLR research aircraft Falcon 20E (http://www.dlr.de/FB/OP) in nadir viewing arrangement. The transmitter is based on a Nd:YAG pumped, injection seeded KTP-OPO (Optical Parametric Oscillator). The Nd:YAG laser is operated in the single longitudinal mode with 220 mJ per pulse at 100 Hz. Half of the fundamental output at 1064 nm is converted to the second harmonic, serving as the pump for the OPO, which produces 18 mJ per pulse at 925 nm. The remaining pump laser radiation is used for atmospheric backscatter measurements. A spectral purity of more than 99% is mostly achieved during in-flight operation; the online frequency is controlled for each shot by use of a water vapor absorption cell. Three locking loops maintain a stable wavelength operation, the exact wavelength information is later needed for the calculation of water vapor concentrations. The back-scattered photons are collected by a Cassegrain telescope

with an aperture of 35 cm and a field-of-view of 2 mrad. The received radiation is split into separate polarization channels at 1064 nm and at 532 nm for the aerosol measurement and the on-line and off-line signals at 925 nm for the water vapor measurement. Background radiation is suppressed by a 1 nm interference filter. Airborne measurements in the 925 nm spectral regions allow to cover the range of typical concentrations from the PBL to the upper troposphere with typical vertical and horizontal resolutions of some 100 m to 1 km and few km to about 10 km, respectively. The nadir-viewing configuration partially compensates the range-dependent (r^{-2}, r: range) signal decrease by the (on average) exponential downward increase of the H_2O-absorption. Mesoscale structures and large humidity gradients near transition zones can thus be resolved throughout the troposphere. A detailed assessment of the measurement accuracy is given by Poberaj et al. [2002]. Uncertainties in the water vapor retrieval stem both from systematic and statistical errors. Main sources of systematic errors are the uncertainty in the determination of the water vapor absorption line cross section (5% estimated uncertainty), laser spectral impurity (1-2%), atmospheric temperature uncertainty (<1%), and the Rayleigh-Doppler absorption line broadening (<1.5% after correction). They sum up to about 5% in total. The statistical error of a DIAL measurement is controlled by the horizontal and vertical data smoothing. For comparison the spatial resolution of the DIAL sections is adapted to the ECMWF resolution, the resulting statistical error remains well below 10%.

The aerosol properties are given as particle backscatter ratio, defined as the total- divided by the molecular backscatter coefficient $R_\lambda = (\beta_{p,\lambda}+\beta_{m,\lambda})/\beta_{m,\lambda}$ (λ denoting the

wavelengths). The color ratio CR = $\beta_{532nm}/\beta_{1064nm}$ is used as an indicator for the effective particle size [Wirth et al., 1999] and the depolarization ratio $\delta_{p,\lambda} = \beta_{p,\lambda,\perp}/\beta_{p,\lambda,\parallel}$ provides the particles' asphericity. The uncertainties in aerosol layers are below 3%, 5% and 10% for R_λ, CR and $\delta_{p,\lambda}$, respectively. The resolution of the backscatter ratio depends on the aerosol optical depth and typically is about 100 m horizontally and some 30 m vertically.

2.3. Meteorological Analyses and Trajectory calculations

The employed synoptic charts and trajectory calculations are based on T511/L60 operational analyses of the European Centre for Medium Range Weather Forecast (ECMWF). At this spectral resolution, the analyses are interpolated onto a regular 0.5°×0.5° latitude-longitude grid; 60 hybrid-pressure levels span from the earth's surface up to 0.1 hPa (ECMWF, 1999). The backward trajectories were calculated with the **La**grangian **An**alysis **To**ol LAGRANTO, developed at the ETH Zürich by Wernli and Davis (1997). They are driven by 6 hourly ECMWF-analyses, interpolated to an incremental time step of 1h and allow for the tracking of various meteorological parameters along the flow.

3. Observations

3.1 Synoptic Conditions

Figure 1 depicts the water vapor mixing ratio q and the geopotential height Φ on pressure levels in the upper troposphere (300, 400 hPa), and the barycenter of the atmosphere (500 hPa) on 14 March 2004, 1200 UT. Transitions between different air masses, transport, and the vertical distribution of water vapor in these charts is clearly linked with the large scale flow pattern, reflected by the Φ-contours. Large q-gradients, frequently associated with upper level fronts, indicate sign-changes in vertical transport, driven by baroclinic adjustment near the jet streams. Coherent vortices appear as regions of closed Φ-contours.

Figure 1

Three climatic regimes are evident in the q-analyses: the meandering planetary wave at mid latitudes with alternating pre-/post-frontal advection of humid/dry air along the flow, humid tropical air masses roughly south of the sub-tropical jet (STJ) at roughly 10-20°N, and in between an irregular sub-tropical transition zone. The large scale flow near the northern flight leg is characterized by the Azores-anticyclone in the west, a trough along the NW African coast and a cyclone over Gibraltar in the north-east. The flight roughly went along the axis of the trough which is associated with an intrusion of dry stratospheric air on its cyclonic shear side. The southern leg crosses the transition from high to low water vapor regions, which is located more southerly at 400 hPa than at 300 and 500 hPa. This signature of the water vapor distribution reflects the tropical Hadley cell which will be discussed below. The vertical humidity decrease is illustrated by use of equal color scales for

all pressure levels. Taking 0.06 g/kg (100 ppmv) as a threshold for stratospheric air (transition to dark green in Fig 1), the hygropause is located above 200 hPa in the tropics and in regions of large scale frontal upwelling, while it typically reaches down to below 400 hPa on the cyclonic shear side of the planetary wave as recently described by Flentje et al., (2005) and references therein.

Owing to sub-tropical subsidence only few clouds occur in the flight path as revealed by Meteosat 8 imagery in Figure 2. Cumulonimbus clouds in the intertropical convergence zone (ITCZ) NE of Brazil, a narrow band of cirrus at about 15°N, post frontal low clouds along the NE African trough and PBL top clouds. Clearly distinguishable from clouds, dust (grayish color) from the African continent is transported across the Atlantic by north easterly trade winds.

Figure 2

3.2. Lidar Measurements

The DIAL-transit on 14 March 2004 is split into 2 segments of about 3000 km each. The water vapor q and the particle backscatter R vertical sections along the flights are displayed in Figure 3, in which low values are emphasized by logarithmic scales. At a resolution of 500-700 m vertically and roughly 3 km horizontally the random error mostly is below 5-10% and gradients are largely maintained. Water vapor mixing ratios cover three orders of magnitude and exhibit complex structures and large gradients. While no correlation is found between water vapor and backscatter ratio in the tropical flight leg, q and R are negatively correlated in the sub-tropical/mid-latitude region. Enhanced backscatter ratios are often found in stratospheric intrusions at mid-latitudes and may originate from long-range transport of lower tropospheric particles injected into the stratosphere by high-reaching,

Figure 3

frontally amplified convection. In the tropics no intrusions or particle layers are observed above 4 km while the lower troposphere is loaded with dust from the African continent.

3.2.1. Flight: Fernando de Naronha – Cape Verde Islands

Near the equator, water vapor mixing ratios q ≈ 1 g/kg reach up to about 8 km. Towards the northeast, the top of this humid layer slopes down to about 4 km near the Cape Verde Islands (23°W, 16°N) and according to ECMWF analyses extends till 20°N. Above 8 km, another humid layer with q ≈ 0.2-0.6 g/kg spreads out horizontally from the equator till 15°N. These layers constitute the lower and upper branch of the Hadley circulation, a climatological large scale skew-meridional circulation cell driven thermally by convective upward and then northward motion near the equator (at low solar zenith angles, SZA) and subsidence in the sub-tropics. The skewness of the Hadley cell is due to the deflecting Coriolis force. The cell is moreover not continuous in zonal direction but associated to the intermittent development of the ITCZ. 7-day back-trajectories ending at different locations within the DIAL curtain trace the traversed air masses back to different origins. Thus, the seemly coherent humidity feature actually is composed of quite different air masses which intersperse each other due to large wind shears. As the flight has not been quasi-Lagrangian (parallel to streamlines) a considerable transport component is perpendicular to the plotted plane. Selected back-trajectories ending at different pressure levels along the flight path are depicted in Figure 4, color-coded with temperature as altitude information. According to these trajectories, air in the tip of the upper water vapor layer, at 300 hPa (≈ 9.6 km) between 9 and 12°N, is subject

Figure 4

to the Hadley circulation. The dry air north of the layer (and below it) emanates from the eastern Pacific upper troposphere and finally subsides southward to the flight section. It exhibits upper tropospheric water vapor mixing ratios around 0.05-0.1 g/kg. The slightly drier air near 3-5°N (@ 300 hPa) originates from the Amazonian region and circles around the Bolivian high towards the mid-Atlantic. The Hadley circulation is evident up to 150 hPa (≈ 14 km), above 150 hPa all back-trajectories remain above the tropopause. This is also in line with the ECMWF analysis of water vapor, displayed up to 18 km in Figure 6 and points up the vertical SW→ up → NE → down → SW circulation. The lower humid layer exhibits q > 2 g/kg and is advected from central Africa by north-easterly trade winds. After the laser beam penetrated about 3-4 km into this lower layer, the H_2O absorption line saturates (i.e. the radiation at the line wavelength is completely absorbed), thus the region below is masked in Figure 3. The decrease of q at the layer's top by an order of magnitude within few 100 m may even be smoothed by the vertical resolution of the DIAL data. The large gradient is a result of shear-induced stretching-thinning of the transition zone between the lower tropical and the on-sliding Pacific air mass.

3.2.2. Flight: Cape Verde Islands – Spain

Along the West African coast (2nd flight leg) different dry and humid air masses are stirred to a complex water vapor distribution. The moist (q > 2 g/kg) maritime PBL covers the lowest 1.5 - 2 km, only inside the Gibraltar cyclone upward-spiraling motion lifts high humidity up to 4 km. Directly above the lifted PBL, a narrow intrusion of UT/LS air (Appenzeller and Davies, 1992) tilts downward and southward from NW-Morocco towards the Canary Islands (≈ 30°N) with low H_2O mixing ratios

below 0.1 g/kg. It is captured by the ECMWF analyses as a thin dry tongue across the flight path near 35-37°N at 500 to 300 hPa, respectively (Fig. 1c). Above the intrusion, a bean-shaped humid air mass is observed and extends till the southern edge of the section. According to backward trajectories shown in Figure 5 its upper part emanates from the Caribbean lower troposphere (LT) while the lowermost part is tracked back to the central Pacific LT. Both parts circled the Azores anticyclone, whereby they were lifted and finally subsided southward as indicated by the right dashed arrow in Fig. 3. A dry layer ($q \approx 0.1$ g/kg) between the bean-shaped air mass and the PBL also originates from the Pacific but at higher altitudes as indicated by about 30 K higher temperatures at the back-trajectory's start. The air inside the dry intrusion, according to back-trajectories, was rapidly lifted by a cyclone south of Greenland to a level where the wind sharply sheared towards the south and then flew along the storm track within 3 days (500 hPa) from Canada to Gibraltar. Finally, it spiraled cyclonically downward by 2-3 km to the observation point while simultaneously the adjacent air directly north of the intrusion spiraled upward in the cyclone by about 2–3 km. It is evident that the narrow dry intrusion is generated by cyclonic interleaving of pre- and post-frontal flows inside the cyclone and that the strong shear zones separate air masses with substantially different q-content and source areas.

Figure 5

The backscatter ratio along this section (Fig 3, panel A) shows an aerosol layer below 4 km altitude extending from the tropics beyond 16°N , the 500 m thick maritime PBL below and thin tilted aerosol filaments along the axis of the UT/LS intrusion between 25°N and 35°N. The aerosol layer over the central Atlantic

originates from the African continent ($v_{wind} \approx$ 5-10 m/s @ 700-850 hPa, 0-10°N during 8-14 March 2004 corresponding to a transport of 400-1000 km/d) and was also observed by the Aqua satellite (http://aqua.gsfc.nasa.gov). According to the lidar backscatter-, color- (not shown), and depolarization ratios (not shown), the particles are solid and of sub-micron size. The CR increases from $\beta_{532}/\beta_{1064} \approx 1$ at the base of the dust layer to $\beta_{532}/\beta_{1064} \approx 1.7$ at it's top; simultaneously δ_p decreases from $\delta_{532} \approx$ 30% to 10%, indicating increasing sizes towards the base of the layer – i.e. gravitational sedimentation. Its optical depth varies between 0.03 and 0.04 at 1064 nm and around 0.05 at 532 nm. The particles inside the UT/LS intrusion exhibit similar color ratios ($\beta_{532}/\beta_{1064} \approx 1.7$) but significantly lower depolarization ($\delta_{532} \approx$ 9% compared to 13%) as those observed inside intrusions over the northern Atlantic in 2002 [Flentje et al., 2005], which most likely originated from forest fires.

4. Comparison with ECMWF Analyses

In Figure 3, the DIAL water vapor sections from 14 March 2004, 1100-1400 UT and 1630-1900UT are compared to operational ECMWF T511/L60 analyses. Albeit at ECMWF the analyses have already been interpolated from their original reduced Gaussian grid to a regular lat-lon grid and thereby lost some resolution, in tropical regions this is only a small effect. Since the operational analyses are by default available and used for scientific studies we compare these humidity fields. In the horizontal the DIAL data are averaged to the analyses' resolution and the analyses are interpolated linearly in space and time to the DIAL profiles along the flight path.

In the vertical the DIAL data are extracted at the ECMWF sigma-levels since vertical smoothing degrades the DIAL vertical resolution below the spacing of the sigma-levels. However, the effective vertical resolution of the ECMWF fields firstly is reduced by numerical diffusion in the Semi-Lagrangian representation of the model. Secondly, since the aspect ratio of vertical to horizontal atmospheric scales is small, structures tilted in sigma-coordinate space are blurred vertically by the far larger horizontal averaging over a grid mesh. The combined impact on resolution is assessed differently but it actually leads to an apparently degraded vertical model resolution corresponding to the smoothed DIAL data which thus may be chosen such that observed small scale tilted features closest resemble those in the analyzed fields.

The water vapor distribution along the flight across the central Atlantic is reproduced in remarkable detail by the ECMWF analyses. Panel D of Figure 3 shows the difference q_{ECMWF} - q_{DIAL} in water vapor normalized to the ECMWF values. The medians of analyzed and observed water vapor mixing ratios, as a measure of the bias between both data fields, differ by less than 10%. The dynamical features which show up in water vapor occur in the analyses only slightly shifted to where they are measured. However, this still induces large relative differences if associated with strong gradients as these are particularly sensitive to small spatial shifts. Rapid temporal development is another major source of deviations because its non-linearity cannot be captured by the linear interpolation between the analysis times. For comparison, contours in percentage of q-change between the 6-hourly analyses interpolated to the measurement time and location is overlayed to the plotted

difference. In panel E the interpolation error between an analyzed field and that interpolated from the ±6h fields is shown which proves that large deviations are mostly associated with rapidly changing features and thus obviously are not due to analysis errors but rather to principal limitations inherent in the comparison of meteorological fields at temporally and spatially finite resolution. By post-processing with hourly storage of the data fields the interpolation errors may be reduced significantly. On large scales the water vapor distribution is largely determined by the model transport rather than constrained by assimilated H_2O data. Therefore, particularly with respect to the comparatively large 6-hourly changes, a much better agreement may not to be achievable. The agreement is slightly worse if the DIAL data are averaged horizontally to an ECMWF equivalent resolution rather than maintaining a DIAL resolution where observed feature resemble each other closest. The differences distribution thereby is affected such that larger deviations occur less but smaller deviations (< 50%) are increased. Additionally, the differences between the analyzed q-fields at a given time and the average of the respective later (+6h) and earlier (-6h) analyses are shown as a measure of the non-linearity of the temporal development. This proves even more clearly the coincidence of large observation-analysis-deviations with the temporal development which can not be exactly duplicated on sub-time-step timescale.

The agreement of analyzed and observed water vapor mixing ratios in specific structures of course becomes the poorer the smaller the scales are, obviously being a matter of resolution of physical processes in the numerical scheme. It is noteworthy that the variability of the PBL depth in the north leg seemly cannot be

captured as accurately as the variability around the stratospheric intrusion although the latter is dynamically much more intense and similarly changeful (see contours in Fig 3D). Particularly large deviations are also found in the transition zone between the lower tropospheric humid air and the up-sliding dry Pacific air in the centre of the Hadley cell at 6 km, 10°N where again the temporal change is large but dynamics (i.e. wind speed and -shear) are relatively weak (as at the PBL top during the 2nd flight). Generally during the 2nd flight above 4 km relatively good agreement is found although the dynamical processes there are most intense as indicated by the temporal q-changes. This indicates a tendency toward better representation of dynamically more intense processes in the ECMWF analyses as long as special scales remain well resolved. Actually, this tendency may be plausible if transport largely determines the analyzed water vapor distribution, because there may be more significant data to assimilate and constrain the model in dynamically active regions and model results generally tend to be more robust in space in dynamically active regions than with weak gradients.

Figure 6

Figure 6 shows the frequency distributions of the calculated differences (q_{DIAL} - q_{ECMWF})/q_{ECMWF} for both flights, respectively. The half-width of the distribution amounts to roughly +20%/-30% deviation. Its skewness, the somewhat larger frequency of moderate negative deviations ($q_{DIAL} < q_{ECMWF}$) occurs particularly clear in the first leg because mainly the upper troposphere, where ECMWF is a bit too humid, was compared. This restriction is only due to missing lidar data in the very humid lower troposphere (absorption-line saturation). The enhanced frequency of larger positive values indicates that DIAL values q_{DIAL} tend to be considerably larger

than q_{ECMWF} where q_{ECMWF} is small and q_{ECMWF} rarely is much smaller than q_{DIAL}. In other words, in very dry regions ECMWF analyses do not fully capture the very low humidity values, particularly in the UT (see Ovarlez and v. Velthoven, 1997). This is also shown by the q_{ECMWF}-q_{DIAL} scatter plots in Figure 7 where the lowest mixing ratios (UT) tend to be below the y = x line (left panel) while at lower- to mid-tropospheric levels a linear fit (not shown) indicates slightly higher DIAL- than ECMWF mixing ratios. The overall agreement in median values within 10% is within the anticipated error bars of both data sets regarding the issues of interpolation, resolution and water vapor absorption cross sections. The latter are determined by own spectroscopic measurements being slightly smaller than in the latest HITRAN compilation (Giver et al., 2000). In Figure 8, individual profiles are compared at positions with small inter profile variability. It confirms that relative spatial shifts (non-linear temporal shifts) are the largest error sources occasionally causing different parts of features to be reproduced with different accuracy. Only, a general tendency to too humid upper tropospheric values is found in the ECMWF analyses while the agreement generally is very close. Restrictively, it must be noted that the DIAL data for this comparison only reach up to 10 km. A detailed comparison in the upper tropical troposphere will be carried out in a following study.

Figure 8

5. Summary

DIAL measurements of tropospheric water vapor and aerosol from Brazil to south Europe in mid-March 2004 are presented and compared to T511/L60 analyses of the ECMWF. The along-flight sections cross the tropical and sub-tropical Atlantic

(5°S–37°N). The climatic zones are clearly distinguishable by the respective water vapor distributions. The water vapor values of the tropical flight leg are governed by the Hadley circulation which reaches up to about 14 km and extends to nearly 16°N. Adjacently, dry sub-tropical subsidence covers most of the middle and upper troposphere up to roughly 20-25°N. The 2nd flight leg exhibits signature of mid-latitude dynamics and complex interpenetration of air masses from lower and higher latitudes. H_2O mixing ratios range from $q \approx 0.01\text{-}0.1$ g/kg in the sub-tropical layer and a stratospheric intrusion to $q > 0.5$ g/kg in lower level air transported up to the UT and q-values larger than 3 g/kg in the PBL and the tropical lower troposphere. On large scales, ECMWF analyses at T511/L60 operational resolution generally reproduce both the dynamical features and the water vapor mixing ratios within the accuracy of the comparison. Larger deviations arise from spatial/temporal shifts, mostly introduced by the limited accuracy of matching both data fields, particularly near sharp gradients and in regions of rapid temporal development. Occasionally, deviations may be induced by inaccurate model transport or water vapor assimilation. Only, a tendency to too humid upper tropospheric values is found in the ECMWF analyses and upcoming will be investigated in detail with data from the TROCCINOX 2004/2005 campaigns in Brazil (http://www.pa.op.dlr.de/troccinox/). The median q-bias between both data fields is below 10% which is within the anticipated error bars of both data sets regarding the issues of interpolation, resolution and measurement uncertainties.

Acknowledgements

We acknowledge the ECMWF for supplying the meteorological analyses. Thanks are to Elias Hólm for helpful comments on the present ECMWF model system. This work was funded by the ESA in the contract no. 10832/03/NL/FF and the European Community in the frame of the TROCCINOX project (EVK2-2001-00087).

References

Appenzeller, C. and H.C. Davies, Structure of stratospheric intrusions into the troposphere, *Nature, 358*, 570-572, 1992.

Andersson, E., E. Hólm and J. N. Thépaut, Impact studies of main types of conventional and satellite humidity data. Proc. 3rd WMO Workshop on "The Impact of Various Observing Systems on Numerical Weather Prediction", Alpbach, Austria, 9-12 March 2004, Eds. H. Böttger, P. Menzel and J. Pailleux. WMO/TD No. 1228, 32-44, 2004.

Brewer, A. W., Evidence for a world circulation provided by the measurements of helium and water vapor distribution in the stratosphere, *Q. J. R. Meteorol. Soc., 75*, 351– 363, 1949.

Bengtsson, L., K. I. Hodges, and S. Hagemann, Sensitivity of large scale atmospheric analyses to humidity observations and its impact on the global water cycle and tropical and extratropical weather systems in ERA40, *Tellus, 56A*, 202-217, 2004.

ECMWF, Increased stratospheric resolution in the ECMWF forecasting system, ECMWF newsletter no. 82, www.ecmwf.int/publications/newsletters/meteorology_articles.html, 1999.

Ehret, G., K.P. Hoinka, J. Stein, A. Fix, C. Kiemle, and G. Poberaj, Low-Stratospheric Water Vapor Measured by an Airborne DIAL, *Journal of Geophysical Research, 104*, D24, S. 31,351-31,359, 1999

Elliott, W.P. and D.J. Gaffen, On the utility of radiosonde humidity archives for climate studies, *Bull. Am. Met. Soc., 72*, 1507-1520, 1991.

Flentje, H., A. Dörnbrack, G. Ehret, A. Fix, C. Kiemle, G. Poberaj, and M. Wirth, Water vapor heterogeneity related to stratospheric intrusions over the northern Atlantic revealed by airborne water vapor, *J. Geophys. Res., 110*, D03115, doi:10.1029/2004JD004957, 2005.

Forster, P. M. de F., and K. P. Shine, Radiative forcing and temperature trends from stratospheric ozone depletion, *J. Geophys. Res., 102*, 10,841– 10,855, 1997.

Gettelman, A., P. M. de F. Forster, M. Fujiwara, Q. Fu, H. Vömel, L. K. Gohar, C. Johanson, and M. Ammerman, Radiation balance of the tropical tropopause layer, *J. Geophys. Res., 109*, D07103, doi:10.1029/2003JD004190, 2004.

Giver, L. P., C. Chackerian Jr., and P. Varanasi, *J. Quant. Spectrosc. Radiat. Transfer, 66*, 101, 2000.

Hólm, E., E. Andersson, A. Beljaars, P. Lopez, J-F. Mahfouf, A. Simmons, and J-N. Thépaut, Assimilation and modeling of the hydrological cycle: ECMWF's status and plans, *ECMWF Technical Memorandum No. 383*, ECMWF, Reading 2002.

Kärcher, B. and S. Solomon, On the composition and optical extinction of particles in the tropopause region, *J. Geophys. Res*., 104, 27441-27459, 1999.

Kiehl, J.T. and K.E. Trenberth, Earth's annual global mean energy budget, *Bull. Am. Met. Soc., 78*, 197-208, 1997.

Kirk-Davidoff, D.B., J.G. Anderson, E.J. Hintsa, and D.W. Keith, The effect of climate change on ozone depletion through changes in stratospheric water vapour. *Nature. 402*, 399-401, 1999.

Leiterer, U., H. Dier and T. Naebert, Improvements in radiosonde humidity profiles using RS80/RS90 radio sondes of Vaisala, *Contrib. Atmos. Phys., 70*, 319-336, 1997.

Manabe, S. and R. Weatherald, Thermal equilibrium of the atmosphere with a given distribution of atmospheric humidity, *J. Atmos. Sci., 24*, 241-259, 1967.

Marseille, G. J. and Bouttier, F., Climatologies of sensitive areas for short-term forecast error over Europe. A EUMETNET-EUCOS study. E*CMWF Technical Memorandum No. 334*, ECMWF, Reading 2001.

Möller, F., On the influence of changes in the CO_2 concentration in air on the climate, *J. Geophys. Res., 68*, 3877-3886, 1963.

Moreau, E., P. Lopez, P. Bauer, A. M. Tompkins, M. Janiskova, and F. Chevallier, Variational retrieval of temperature and humidity profiles using rain rates versus microwave brightness temperatures, ECMWF Technical Memorandum No. 412, 2003 (http://www.ecmwf.int).

Oltmans, S. J., H. Vömel, D. J. Hofmann, K. H. Rosenlof, and D. Kley, The increase in stratospheric water vapor from balloon-borne, frostpoint hygrometer measurements at Washington, D.C. and Boulder, Colorado, *Geophys. Res. Lett., 27(21)*, 3453– 3456. 2000.

Ovarlez, J., and P. van Velthoven, Comparison of water vapor measurements with data retrieved from ECMWF analyses during the POLINAT experiment, *J. Appl. Meteorol., 36*, 1329-1335, 1997.

Poberaj, G., A. Fix, A. Assion, M. Wirth, C. Kiemle, and G. Ehret, All-Solid-State Airborne DIAL for Water Vapor Measurements in the Tropopause Region: System Description and Assessment of Accuracy, *Appl. Phys. B 75*, 165-172, 2002.

Sherwood, S. C., and A. E. Dessler, On the control of stratospheric humidity, *Geophys. Res. Lett., 27*, 2513-2516, 2000.

Shine, K.P. and A. Sinha, Sensitivity of the earth's climate to height dependent changes in the water vapor mixing ratio, *Nature, 354*, 382-384, 1991.

Wernli, H., and H. C. Davis, A Lagrangian-based analysis of extratropical cyclones. I: The method and some applications, *Q. J. R. Meteorol. Soc.*, *123,* 467-489, 1997.

Figure Captions

Fig. 1: Water vapor mixing ratio (g/kg) and geopotential height (m) analyzed at (a) 200, (B) 300 and (c) 500 hPa by the ECMWF (T511/L60) on 14 March 2004, 1200 UT. The Falcon flight path is marked by a white line.

Fig 2: Meteosat 8 image of cloud coverage and dust transport from the central African continent on 14 March 2004, 1200 UT. White: Flight track from Brazil to Germany via the Cape Verde islands and Spain.

Fig 3: Backscatter ratio R (A) and water vapor mixing ratio q in g/kg (B) along DIAL flights on 14 March 2004, 1100-1400 UT and 1630-1900 UT using log color scales. Isolines are pressure. H_2O profiles are averaged over 700 m vertically and ≈ 3 km horizontally. (C): ECMWF T511/L60 operational analysis on sigma levels (~30), interpolated in space and time on the flight tracks. Contours are potential temperature (grey), horizontal wind speed (black) and potential vorticity at 2, 2.5 and 3 PVU. (D): Difference of water vapor mixing ratios $q_{ECMWF} - q_{DIAL}$ from the upper panels on linear color scale with overlayed contours of relative q-change (40%, 100%) between 6UT/12UT (southerly flight) and 12UT/18UT (northerly flight). Note the different altitude range of the ECMWF panel. (E): Difference between 030314 6/18UT mean to 12 UT analysis (southerly flight) and 030314 12 UT/ 030315 00UT mean to 030314 18 UT analysis (northerly flight) as a measure of the non-linearity of the temporal development.

Fig 4a, b: 7-day ECMWF backward trajectories arriving at the DLR Falcon flight track at (a) 300 hPa and (b) 700 hPa on 14 March 2004 12 UTC, color coded with temperature.

Fig 5a, b: 9-day ECMWF backward trajectories arriving at the DLR Falcon flight track at (a) 500 hPa and (b) 700 hPa on 14 March 2004 18 UTC, color coded with temperature.

Fig 6: Frequency distribution of differences $(q_{DIAL} - q_{ECMWF})/q_{ECMWF}$ shown in Fig 3 (lowest panel) along DIAL flights on 14 March 2004, 1100-1400 UT (dashed) and 1630-1900 UT (solid).

Figure 7a, b: Scatter plots of ECMWF and DIAL water vapor mixing ratios in g/kg along the 2nd flight on 14 March 2004. The dashed lines denote y = x. Only ECMWF levels 22-28 (≈ 6-10 km = upper limit of DIAL data) in the left panel (a) and levels 12-20 (≈ 1.5–5 km) in the right panel (b) are included, highlighting the upper and lower troposphere, respectively. The stringing results from individual model levels.

Figure 8: Comparison of profiles of water vapor mixing ratio from resolution-degraded DIAL measurements (dashed) and ECMWF analyses (solid) from the flights on 14 March 2004. Profile locations along the flight track, as indicated in the 3rd panel of Fig. 3 are 4°S, 4°N, 10°N, 13°N (upper panel) and 23°N, 28°N, 31°N, and 33°N (lower panel).

List of Figures

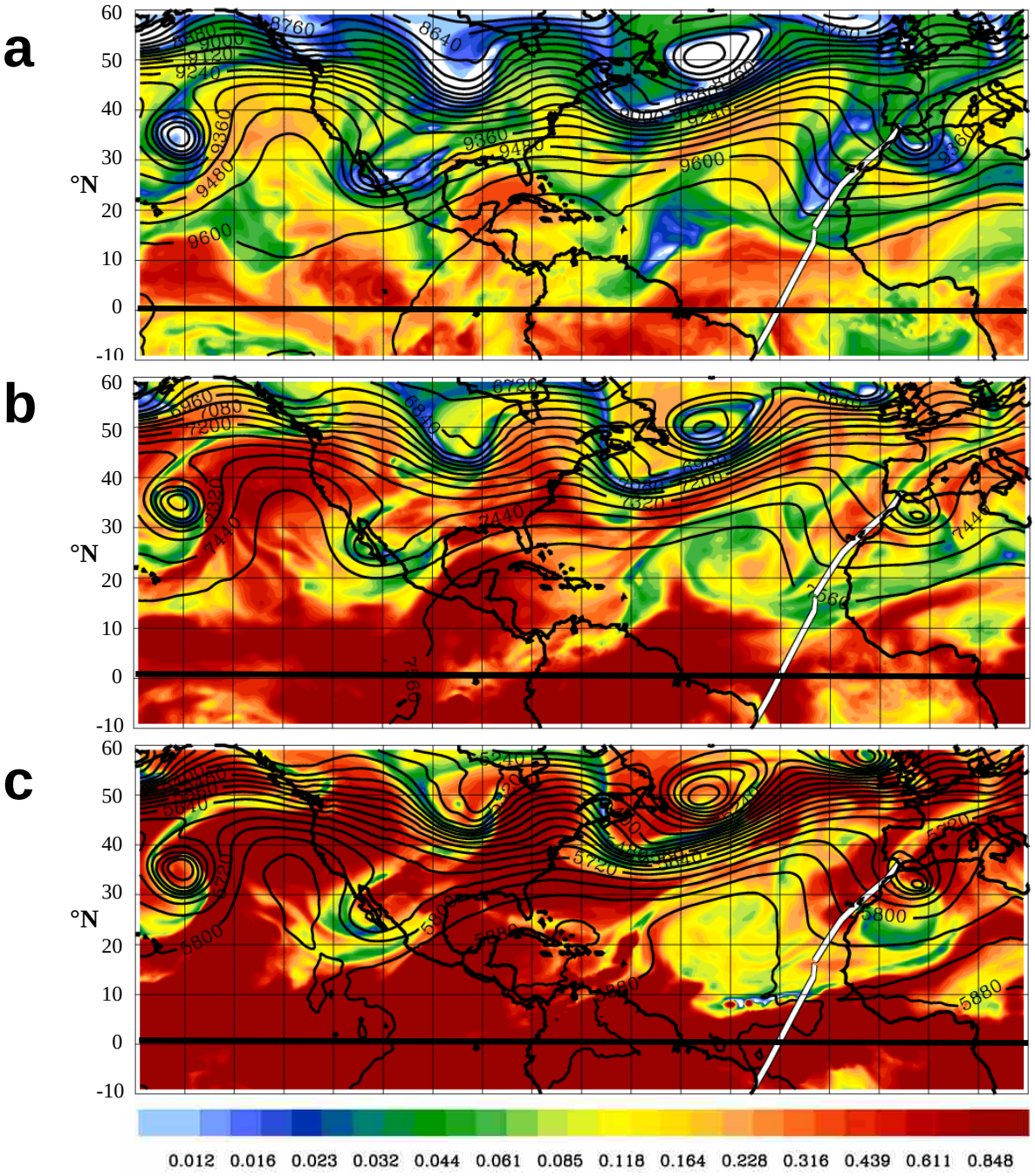

Fig. 1: Water vapor mixing ratio (g/kg) and geopotential height (m) analyzed at (a) 300, (b) 400 and (c) 500 hPa by the ECMWF (T511/L60) on 14 March 2004, 1200 UT. The Falcon flight path is marked by a white line.

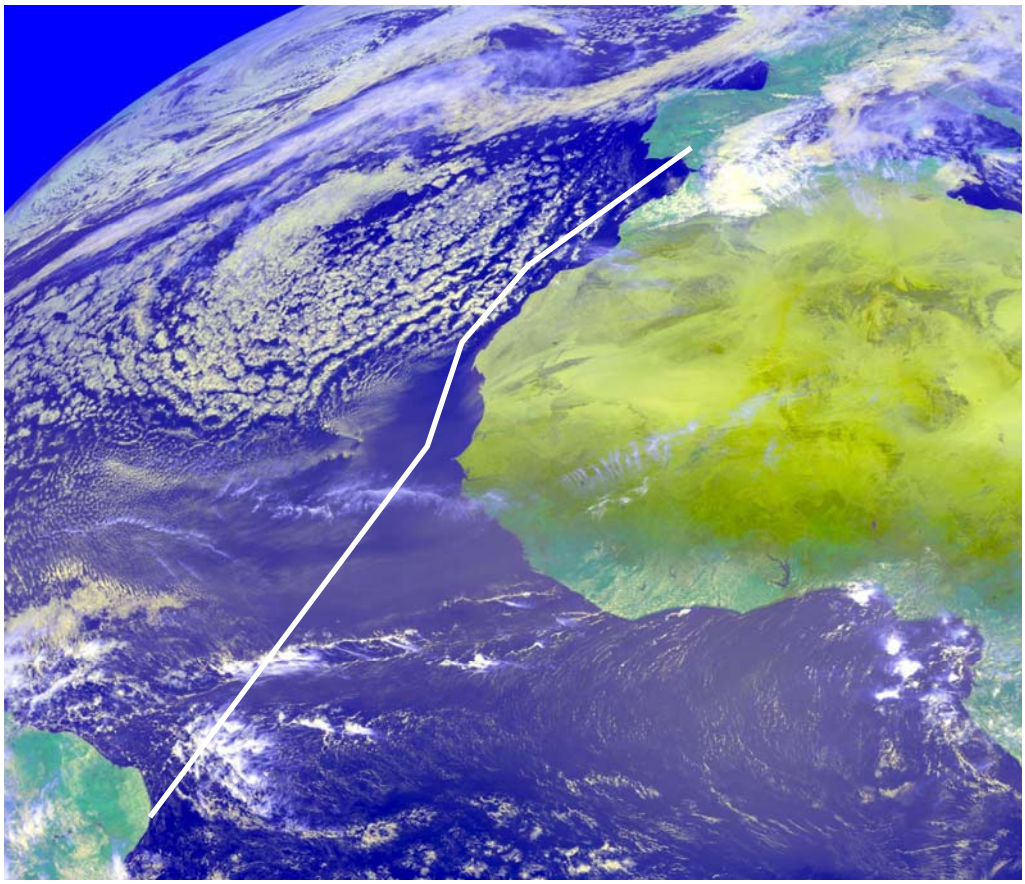

Fig 2: Meteosat 8 image of cloud coverage and dust transport from the central African continent on 14 March 2004, 1200 UT. White: Flight track from Brazil to Germany via the Cape Verde islands and Spain.

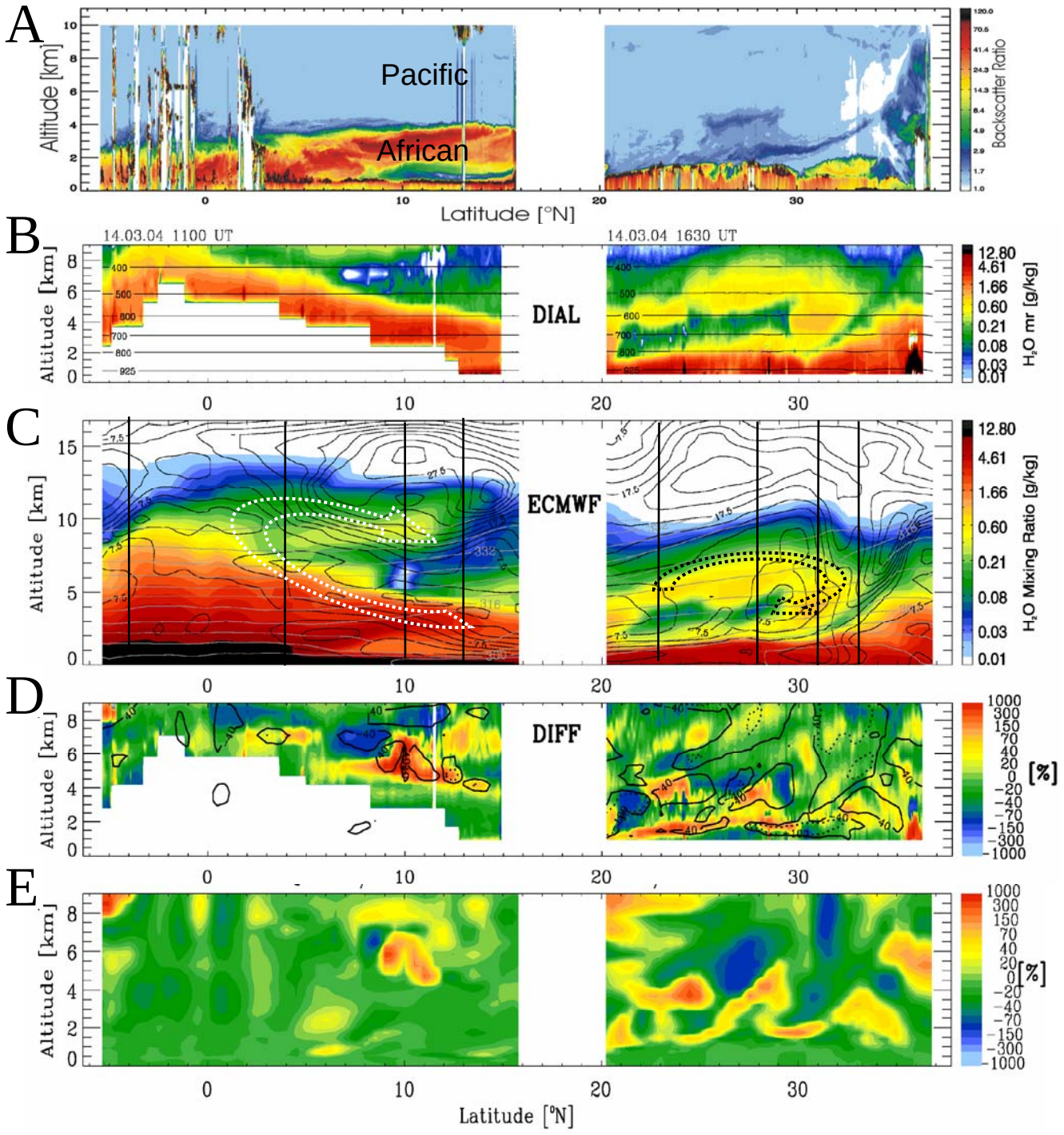

Fig 3: Backscatter ratio R (A) and water vapor mixing ratio q in g/kg (B) along DIAL flights on 14 March 2004, 1100-1400 UT and 1630-1900 UT using log color scales. Isolines are pressure. H_2O profiles are averaged over 700 m vertically and ≈ 3 km horizontally. (C): ECMWF T511/L60 operational analysis on sigma levels (~30), interpolated in space and

time on the flight tracks. Contours are potential temperature (grey), horizontal wind speed (black) and potential vorticity at 2, 2.5 and 3 PVU. (D): Difference of water vapor mixing ratios $q_{ECMWF} - q_{DIAL}$ from the upper panels on linear color scale with overlayed contours of relative q-change (40%, 100%) between 6UT/12UT (southerly flight) and 12UT/18UT (northerly flight). Note the different altitude range of the ECMWF panel. (E): Difference between 030314 6/18UT mean to 12 UT analysis (southerly flight) and 030314 12 UT/ 030315 00UT mean to 030314 18 UT analysis (northerly flight) as a measure of the non-linearity of the temporal development.

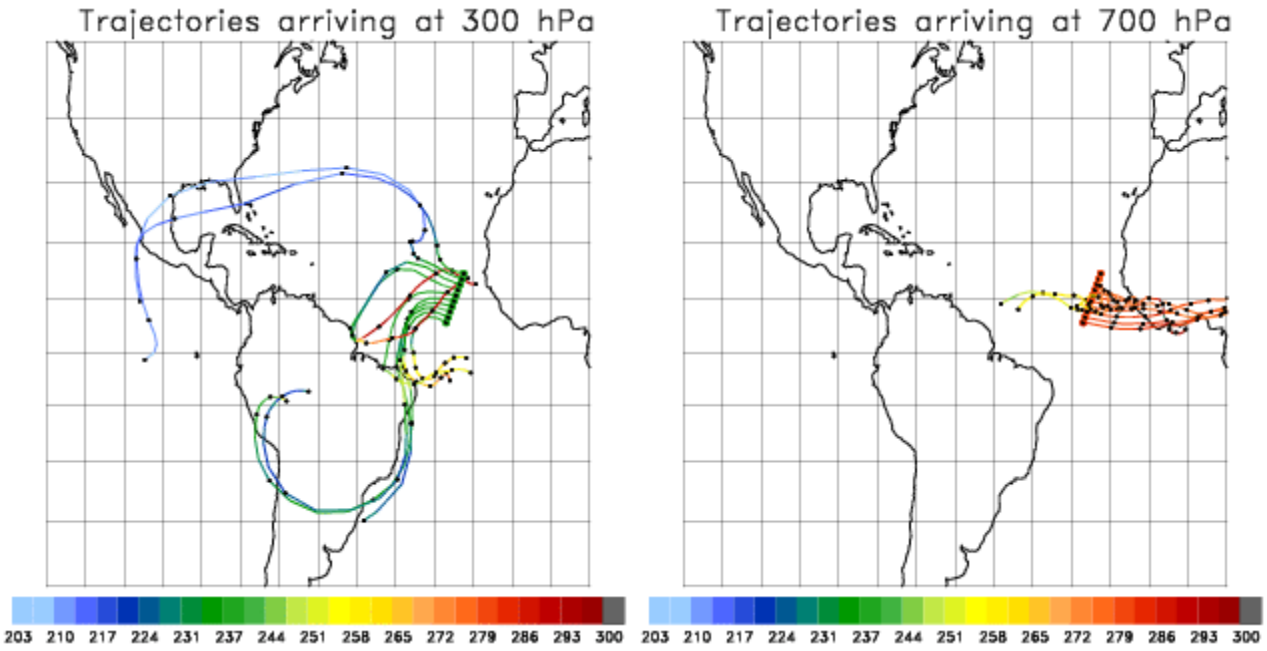

Fig 4a, b: 7-day ECMWF backward trajectories arriving at the DLR Falcon flight track at (a) 300 hPa and (b) 700 hPa on 14 March 2004 12 UTC, color coded with temperature.

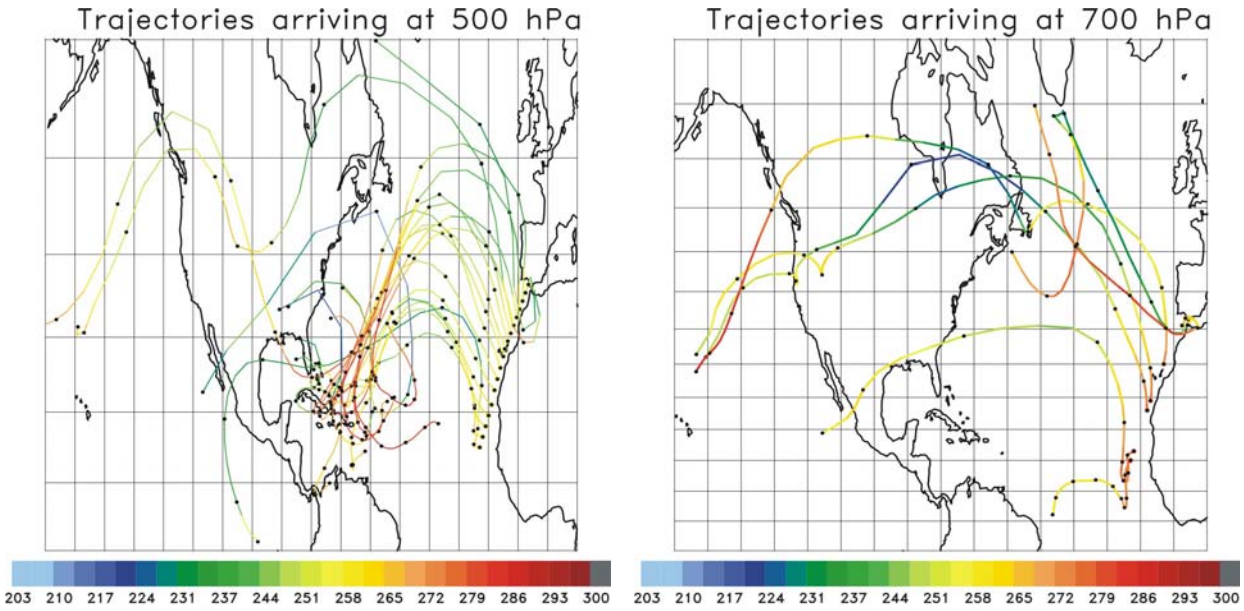

Fig 5a, b: 9-day ECMWF backward trajectories arriving at the DLR Falcon flight track at (a) 500 hPa and (b) 700 hPa on 14 March 2004 18 UTC, color coded with temperature.

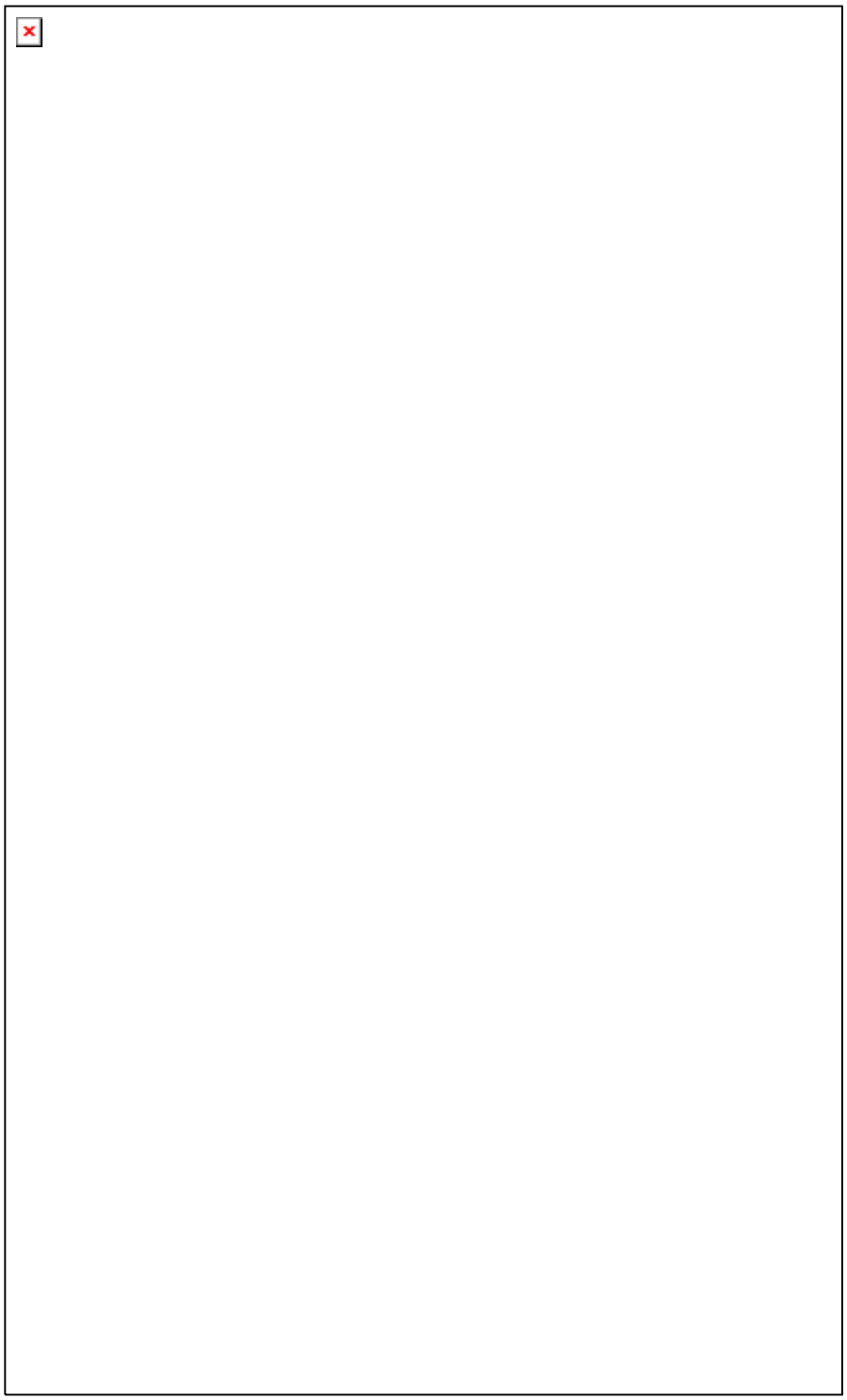

Fig 6: Frequency distribution of differences (q_{DIAL} - q_{ECMWF})/q_{ECMWF} shown in Fig 3 (lowest panel) along DIAL flights on 14 March 2004, 1100-1400 UT (dashed) and 1630-1900 UT (solid).

(a) **(b)**

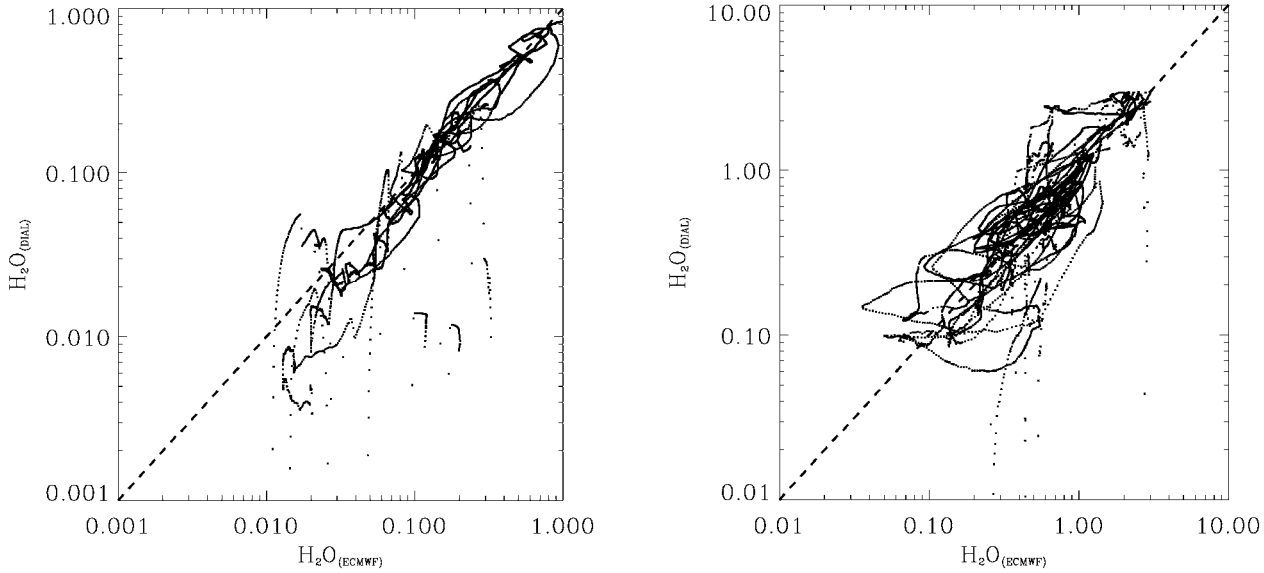

Figure 7a, b: Scatter plots of ECMWF and DIAL water vapor mixing ratios in g/kg along the 2nd flight on 14 March 2004. The dashed lines denote y = x. Only ECMWF levels 22-28 (≈ 6-10 km = upper limit of DIAL data) in the left panel (a) and levels 12-20 (≈ 1.5–5 km) in the right panel (b) are included, highlighting the upper and lower troposphere, respectively. The stringing results from individual model levels.

Figure 8: Comparison of profiles of water vapor mixing ratio from resolution-degraded DIAL measurements (dashed) and ECMWF analyses (solid) from the flights on 14 March 2004. Profile locations along the flight track, as indicated in the 3rd panel of Fig. 3 are 4°S, 4°N, 10°N, 13°N (upper panel) and 23°N, 28°N, 31°N, and 33°N (lower panel).